Technical realisation of an SiPM-based muon detector

von

Erik Ehlert

Bachelorarbeit in Physik

vorgelegt der
Fakultät für Mathematik, Informatik und Naturwissenschaften
der
Rheinisch-Westfälischen Technischen Hochschule Aachen

August 2022

angefertigt am

III. Physikalischen Institut A

Abstract

This thesis describes the design process of a detector for cosmic muons, its key feature providing a spacial resolution. In order to determine the optimal operation parameters for the used SiPMs, the temperature dependency of their overvoltage gets determined and a method for the calibration of the SiPMs is conceptualised. Also, noise characteristics of the SiPMs are investigated to develop suitable boundary conditions for coincidence measurements. Furthermore, the structure of the readout electronics gets established and first parts are designed and tested. As part of the process, the design and production of the detector's casing are described.

Contents

1 Introduction and overview

In the field of particle physics, many different types of detectors exist, each with their own application. An interesting category of detectors are pixel trackers which primary use is to determine where a particle crosses them. Multiple of those trackers can be combined to a hodoscope, from the Greek word for way "hodos" and the word for observer "skopos". Generally, a hodoscope enables to retrace the path of a particle.

In the Physics Institute III A of the RWTH Aachen University, a silicon photomultiplier (SiPM) based muon detector module is currently under development. This module consists of a square scintillating tile and four SiPMs. Experiments are being carried out to enhance the spacial resolution, by comparing the measured light yield of the four SiPMs. To be able to cross-check possible results, a reference detector is needed. This thesis deals with the conceptual design and construction process of this reference detector.

1.1 Detector concept

Today, a common way to detect charged particles are scintillators. These are materials that emit light when such a particle passes them. The produced light pulse then can be detected by a designated read-out electronic. A description of the functional principle of scintillators can be found in chapter 2.

To detect the emitted light pulse of a scintillator, mostly photo multiplier tubes (PMT) were used [1, 2]. But during the last decade silicon photo multiplier (SiPM) became a viable alternative option [3, 4, 5]. They have a similar sensitivity and operate at a much lower voltage of $\sim 30\,\mathrm{V}$ in comparison to the $\sim 1000\,\mathrm{V}$ required for a PMT. Furthermore, SiPMs have a smaller footprint which enables the construction of more compact detectors. Downsides of SiPMs are their high noise and high temperature dependence of all relevant properties, which requires calibration [6]. For this detector an SiPM was chosen as the photon detector. In section 2 the functionality of a SiPM is described in more detail.

With the ability to detect muons, the next function the detector has to accomplish is an x–y resolution. There are many possible solutions to achieve this. In positron emission tomography (PET) the detectors consist of an array of SiPMs, each with their own scintillator directly on top. In those setups, each SiPM is comparable to a pixel of a CMOS camera sensor. This allows for a spacial resolution of down to 1 mm. However, the main goal of this arrangement is a high timing

and energy resolution, both of which are not needed for our detector. The cost per channel and per area covered is also very high [7, 8].

To cover more area, most detectors use larger scintillators that are connected to the readout electronic at their ends or via light guiding fibres. In [5] this was done by embedding fibres into the top side of a square piece of scintillator and the same amount perpendicular in to the under side. To calculate where the particle crossed the scintillator, the brightness at the end of the fibres was measured. An advantage of this configuration is its very simple mechanical design. On the other hand, the electronic readout is more complicated. Since the SiPMs not only need to detect the presence of a light pulse, but its brightness, they need to be even more precisely calibrated. Furthermore, the position reconstruction does get worse at the edges of the scintillator, due to the setup of the fibres.

Instead of fibres inside a scintillator, optically isolated scintillator strips are also an option. These strips get oriented in the same manner: two layers perpendicular to one another. By this, the spacial resolution can be directly controlled by the size of the strips. Also, this setup allows for an easy implementation of coincidence measurements. This means each strip can be read out by two SiPMs and the measured signal can be compared, to minimise false hits due to noise. A drawback is the need for optical isolation of the scintillators. This can be realised by mechanical barriers between the different channels, slightly reducing the scintillating area of the detector [1, 2, 9].

For our detector, the last configuration was chosen. Each of the two layers is divided into 16 strips with a SiPM on each end. Leading to a total of 32 scintillator strips and 64 readout channels.

2 Principles of the used detector elements

To understand the design decisions taken in section 4 and 5, this section deals with the relevant fundamental principles. Hereby, emphasis is put on the parameters and functions, which are important for the operation of the detector. As mentioned in the introduction, for the detection of muons, two main parts are essential: the scintillator that converts the energy from a muon passing it into a light pulse and the SiPM, which converts that light pulse into an electric signal.

2.1 Scintillators

Scintillation is a form of luminescence. It describes the property of a material, to emit light after absorbing energy from radiation. Depending on the type of scintillator this radiation can be high energy photons, neutrons or any charged particle. When this radiation passes the scintillator it may excite electrons to a higher energy level. When the decay of the excited energy level includes a light emitting transition, a photon will be emitted. These photons have, for the majority of scintillators, an energy of around 3 eV, which corresponds to a wavelength of approximately 400 nm [10].
There are two main types of scintillators, organic and inorganic. Inorganic scintillators are ionic crystals. The scintillation effect of these crystals is a lattice effect. Organic scintillators are aromatic hydrocarbon compounds. Here scintillation occurs as a result of excitation of molecular levels. Organic scintillators can be used as a liquid, by dissolving scintillating materials in a solvent, or as a solid in the form of plastic scintillators [11]. Owing to mechanical setup, only solid scintillators are of interest or our application.
Due to non-radiating transitions, the mean energy that is needed to produce a photon is significantly higher than the energy of the photon. Inorganic scintillators usually have a lower energy needed per photon of down to 25 eV, where organic ones need around 125 eV [11].
Other important characteristics of scintillators are the decay constant and the bulk light attenuation length. The decay constant is a parameter for the time that it takes an excited energy level to decay. The decay time gives information on how long a light pulse emitted by this scintillator is. For applications where timing information is important, a low decay time would be desired. Organic scintillators feature a decay time of about 2 ns to 30 ns. Inorganic scintillators have a larger range and, depending on the type, can have a decay time of 5 ns up to 1 µs [12]. The bulk light attenuation length is the distance the scintillation light can travel through

the scintillator, until its intensity is reduced by the factor of e. A long attenuation length is desired, because otherwise the emitted light can't reach the surface of the material, where it could be detected.
Another important difference between inorganic and plastic scintillators is cost and shapeability. Inorganic scintillators are crystals, they are difficult to grow and can not simply be altered to any arbitrary desired shape or size, after their initial production. Plastic scintillators on the other hand are cheaper and can be extruded into any shape and form, cut and machined.

For our detector, plastic scintillators were used. For more information see section 3.

2.2 Silicon photomultipliers

In order to understand Silicon photomultipliers (SiPMs), first its precursors must be understood. In order to do this, this section tracks the steps from a simple photodiode over avalanche photodiodes (APD) to geiger-mode avalanche photodiodes (GAPDs) and finally to SiPMs. This explanation will be kept to a minimum and only discuss matters which are important for the operation of the detector. For further reference please refer to [13], [14] for semiconductor detectors and for SiPM specifically to [15].

2.2.1 Photodiode

A photodiode is a p-n diode, optimised for photon detection. This diode has many interesting and useful properties. For the application as light sensor, the most important property is that if a photon excites an electron into the conduction band inside the depletion zone, the electron and its respective hole can be drifted apart. When this happens, the electron-hole (e-h) pair can not recombine. If the leads of such a diode are connected via an ampere-meter, the current created from this effect can be measured. Since every photon only results in one e-h pair, a large number of photons are needed to result in a measurable effect [13]. Photodiodes are today widely used in the form of photovoltaic cells.

2.2.2 Avalanche photodiode

In order to achieve a higher gain than the gain of $g = 1$ of a photodiode, an external voltage, called bias voltage, can be applied. This voltage increases the electric field strength inside the APD. If the electric field is high enough that the electrons gain

enough energy to create new e-h pairs themselves, an avalanche is formed. In an APD the electric field is only high enough that the electrons of an e-h pair can create new e-h pairs. This results in an avalanche that only flows in one direction. The avalanche leads to a gain of $g = 50$ to 200 [16]. An illustration of this effect is shown in figure 1 on the left. The exact structure of an APD is more complicated than that of a simple photodiode and depends on the application and wavelength it is designed for. The structure and material of an APD also dictates the voltages at which it can be operated.

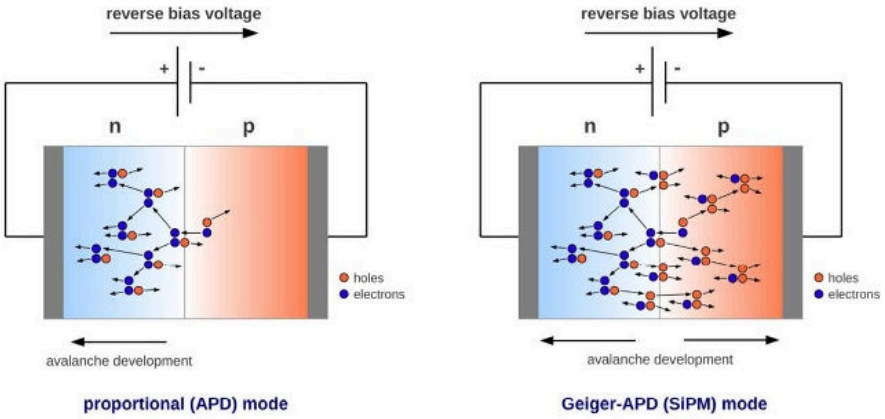

Figure 1: The plots illustrate the building of e-h pair avalanches inside a photodiode. On the left side, a simplified APD is shown. Here the bias voltage is sufficiently high that electrons can excite new e-h pairs. On the right side, a GAPD is shown. Here the bias voltage is greater than the breakdown voltage and the avalanche is self-sustaining. Taken from [15]

2.2.3 Geiger-mode avalanche photodiode

A photodiode can be designed to be operated at voltage levels where even the holes can excite new e-h pairs, then the created avalanche becomes self-sustaining. This has the effect that it can no longer be distinguished between different amounts of photons. Just one e-h pair is needed to trigger the whole GAPD. The voltage at which this occurs is called breakdown voltage. In order to reset the GAPD, the bias voltage needs to be lowered under the breakdown voltage. In most applications, this is done by a resistor in series to the diode. When the avalanche is triggered, the resulting current generates a voltage drop at the resistor, thus lowering the bias

voltage. This process is called quenching. An illustration of the avalanche can be seen in figure 1 on the right-hand side.

The gain of a GAPD can be as high as 10^8 [17]. With the ability to detect single photons, but at the cost of the ability to distinguish between different amounts of photons.

The gain can be controlled by applying different voltages. To calculate this, it is common to split the applied bias voltage

$$V_{bias} = V_{br} + V_{ov} \tag{1}$$

into the breakdown voltage V_{br} and the overvoltage V_{ov}. The gain is proportional to the overvoltage $g \propto V_{ov}$.

2.2.4 SiPMs

To be able to distinguish between different intensities of light, a SiPM is essentially an array of many GAPDs and their quenching resistors, often in the range of a few thousands. One GAPD and its resistor are called a SiPM cell. The different cells are connected in parallel as shown in figure 2. By doing this, the current through the cells is added up. The resulting current is proportional to the number of triggered cells. For lower numbers of simultaneously active cells, the number can be discretely distinguished. If a signal consists of just one fired cell, it is called 1 p.e. (photo-electron equivalent) for two cells it is called 2 p.e. and so on.

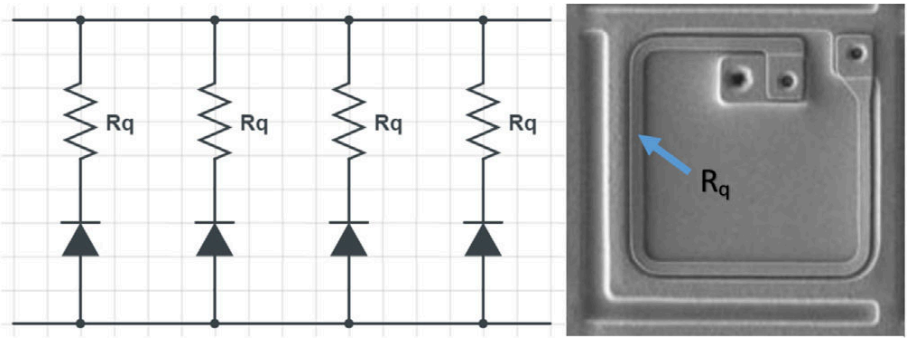

Figure 2: The figure shows a simplified schematic of a SiPM with its GAPDs and quenching resistors R_q. On the right side a microscopic image of a SiPM cell is shown. Taken from [18].

Since a SiPM consists of many small cells, not the whole area of an SiPM is photo-sensitive. The more cells an SiPM has for a given area, the lower gets the

proportion of photo-sensitive to insensitive area, called the geometric fill factor. This fill factor affects the photo detection efficiency (PDE) of a SiPM and is usually around 50 % to 75 % [19].

Other factors the photon detection efficiency depends on include the avalanche probability, the quantum efficiency of the GAPDs, and the coating of the SiPM's surface. The overall PED follows from these factors and depends on the wavelength of the incoming photon. The PDE of an J–Series SiPM from onsemi is shown in figure 3. There it can be seen that the PDE also increases with higher overvoltage.

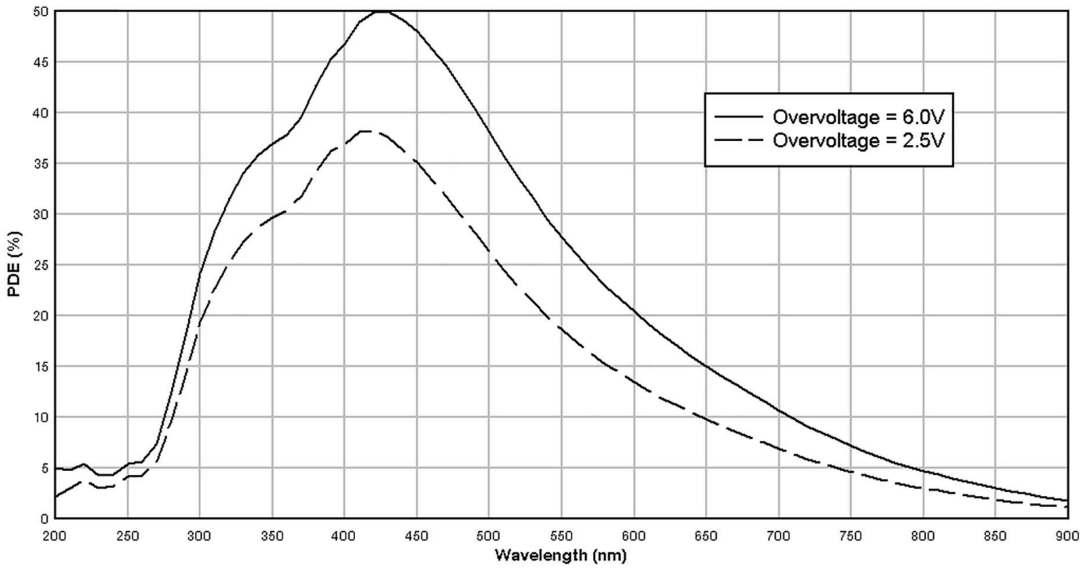

Figure 3: In this plot, the photon detection efficiency (PDE) of a J–Series SiPM from Onsemi as a function of wavelength can be seen. The function is plotted for an overvoltage of 6 V and 2.5 V, respectively. Taken from [19].

2.2.5 Noise and temperature dependency of SiPMs

An avalanche inside a GAPD can, instead of by a photon, also be triggered by a thermally excited electron and cause the cell to trigger. The signal created from this can not be distinguished from a cell triggered by a photon. Since this is a volumetric effect, the rate of this noise increases with SiPM size and is highly dependent on the overvoltage. Onsemi reports the rate of their J–Series SiPM to be $50\,\mathrm{kHz\,mm^{-2}}$ at $V_{ov} = 2.5\,\mathrm{V}$ and $150\,\mathrm{kHz\,mm^{-2}}$ at $V_{ov} = 6\,\mathrm{V}$ [19].

Another noise characteristic of SiPMs is optical crosstalk. This effect occurs when a photon is emitted by an avalanche. Such a photon can then trigger a neighbouring cell. This effect can happen in a cell triggered by a photon or by thermal noise, making it possible to get thermal noise signals higher than 1 p.e. The likelihood of optical crosstalk, in current generation SiPMs, is around 10 % to 25 % and, same as the thermal noise rate, rises with higher overvoltage.

During an avalanche, a charge carrier can get trapped by impurities or defects inside the semiconductor volume. These can, when released, trigger second avalanches the so-called afterpulses. This usually happens a few nanoseconds after the initial pulse [20]. A plot of the signal the different types of noise create is shown in figure 20.

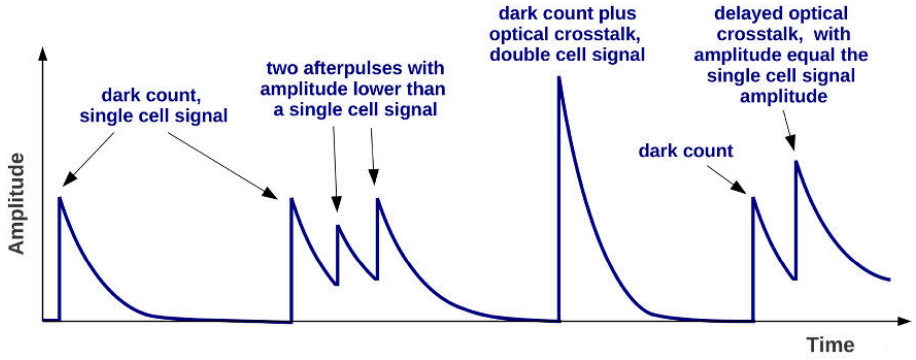

Figure 4: Plotted representation of the noise output of an SiPM. All effects mentioned in the text above and combination of those can be seen. Taken from [15].

The breakdown voltage of GAPDs and respectively of the SiPMs is temperature dependent and increases with higher temperature:

$$V_{br} = V_{br}(T_0) + b(T - T_0) \tag{2}$$

with $b > 0$, for J–Series SiPMs from onsemi this factor is $21.5\,\mathrm{mV\,°C^{-1}}$ [19]. This means that in order to get a constant gain, across different temperatures, the bias voltage needs to be adjusted accordingly. Furthermore, the breakdown voltage $V_{br}(T_0)$ varies across even the same type of SiPMs, due to manufacturing variance. In order to generate consistent data with a detector utilising multiple SiPMs, all of them need to be individually calibrated.

3 SiPM and scintillator light yield optimisation

For this detector, the MicroFJ–30035 SiPM from onsemi [19] is used. A few of its characteristics have already been mentioned in section 2. Figure 3 shows its PDE for different wavelengths. In order to detect as many photons as possible, the emitted photons of the used scintillator must match the absorption bandwidth of the SiPM. The optimal wavelength for the used SiPM is in the vicinity of 420 nm [19]. For the scintillator two choices were available, the BC–404 and BC–408 from Saint–Gobain [21]. These plastic scintillators feature a similar light output. BC–404 has a faster decay time but shorter light attenuation length as BC–408. The emission spectra of both scintillators are shown in figure 5.

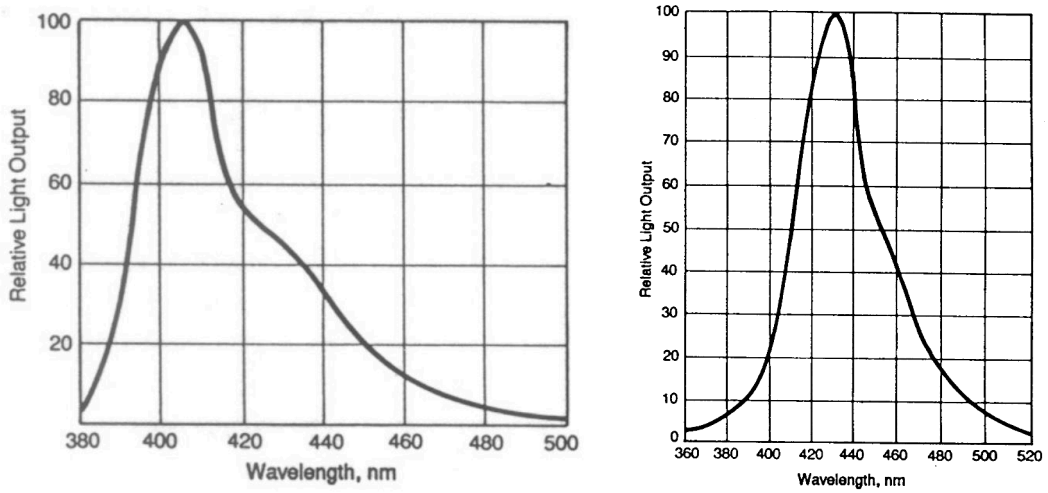

(a) Emission spectra of BC-404 scintillator.

(b) Emission spectra of BC-408 scintillator.

Figure 5: Emission spectra of BC–404 (left) and BC–408 (right). The maximum of BC–404 is at 408 nm and the maximum of BC–408 at 425 nm. Taken from [21].

If the emission spectra are compared to the PDE of the SiPM, the BC–408 is a better match. Since the emission and PDE maxima overlap. Furthermore, BC–408 features a longer attenuation length of 210 cm.

To maximise the amount of light that reaches the SiPM, light guiding fibres are embedded into the scintillator. Such a fibre traps light along its length and emits it at its ends. This is achieved by total internal reflection of the light inside the

fibre. In order for light to get trapped inside the fibre it needs to enter it at a shallow angle. Because not all photons emitted by the scintillator hit a fibre in a suitable angle, the scintillator gets wrapped into a diffuse reflecting, cloth like, material called Tyvek® [22], made by DuPont. The wrapping of scintillator in reflective material is also done to generally keep the emitted light inside. The advantage of a diffuse reflecting material in comparison to for example a reflective foil is that the reflection angle of the light changes [23]. By this, the probability of photons to get trapped inside the fibre is increased. In [24] it was found, for a similar setup, that the wrapping of the scintillator with Tyvek resulted in a higher light output by a factor of two, in comparison to a blank scintillator. Another advantage of the fibres is their typically larger attenuation length. For more information on how the fibres trap light and how it propagates inside, a detailed description is given in [23].

In our setup, each of the fibres is connected to an SiPM at one of its ends. With this configuration, half of the light is lost since it will exit the fibre at the end where no detection takes place. To counteract this, the open end of each fibre is also covered by Tyvek. This results in a light yield improved by about 50% [25], depending on the type of fibre and the proper attachment of the "end-cap" Tyvek. This improvement is especially dependent on the attenuation length of the used fibre, because the reflected light needs to travel the whole length of the fibre to reach the SiPM.

The usage of fibres is extremely important, since the cross-section of the scintillator is a lot larger than the SiPM. Without it, only a fraction of the emitted photons would reach it. The best way of mounting the fibres is to glue them into grooves with optical cement [24]. For our setup, it was chosen to embed two fibres into the scintillator, one on the left and one on the right side, respectively. A similar setup was tested in [11] and showed promising results.

Since the emission and PDE of the scintillator and SiPM are already compatible a clear light guiding fibre would be more optimal. However, due to global supply chain crisis caused among other things by the pandemic, only wavelength shifting fibres were on hand. This problem of out-of-stock items and long lead times was often encountered during the build process. Especially for the design of the readout electronics a few compromises had to be made.

A wavelength shifting fibre absorbs light and emits light of a longer wavelength. For our application we had to take the fibre Y–11 made by Kuraray. Which absorbs blue light and emits green light. The fibre has a light attenuation length of 3.5 m, making it a suitable light guide in comparison to BC–408 with its attenuation length

of 0.21 m. The emission and absorption spectra of the Y–11 are shown in figure 6. Here it can be seen that it is a good match with the BC–408, with its absorption peak at 430 nm. Suboptimal is the emission, with its peak at 473 nm and most of its spectra at even higher wavelengths. With this setup, under optimal conditions and neglection of attenuation, a maximal overall PDE of approximately 42% at $V_{ov} = 6\,\mathrm{V}$ and 30% at $V_{ov} = 2.5\,\mathrm{V}$ can be achieved. This coarse evaluation was made by multiplying the emission and absorption probabilities at the peak of the respective spectra.

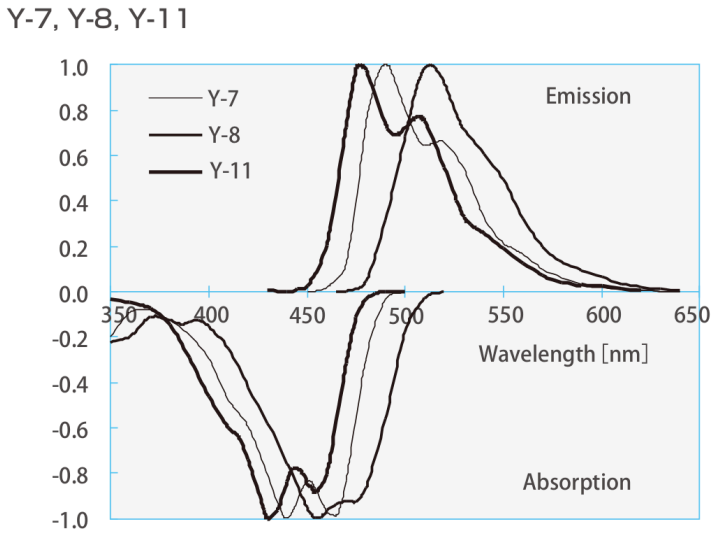

Figure 6: Emission and absorption spectra of Y–7, Y–8 and Y–11 wavelength shifting fibres from kuraray. For the detector, Y–11 fibres were used. Taken from [26].

4 Mechanical design

This section explains the mechanical design of the casing and the scintillator. The main purpose of the casing is to hold the scintillator strips in place and to keep external light from entering the scintillator or from reaching the SiPM. Furthermore, it should hinder light from one scintillator to reach a neighbouring one and induce undesired optical crosstalks between different channels.

4.1 Shape and size of the scintillator strips

The final hodoscope needs to have an active area of about 50 cm × 50 cm [27]. The BC-408 material from which the scintillator strips were cut are 5 mm thick. It was chosen to have 16 channels per layer, as an optimal match between a reasonable resolution and a two-based number of channels [28]. Between every strip, a metal sheet with a thickness of 1 mm is placed to optically separate them. A layer of Tyvek, the material in which the scintillator strips are wrapped, was measured to be 0.32 mm thick, allowing for some clearance. Resulting in a maximal width of 29.7 mm for the scintillators. Thus, one scintillator strip will have a size of 500 mm × 29.7 mm × 5 mm. This leads to a geometric efficiency of 95.0% for one layer. Since two layers are combined to enable a x–y resolution, the total geometric efficiency goes down to 90.3%.

The wavelength shifting fibres were glued into the sides of the scintillator strip. For this, 2 mm deep and 1 mm wide grooves were cut in the middle of the long side-faces of each strip. A sketch of this cross-section is shown in figure 7. After the fibres were glued into place, their endings were cut off and the faces of the scintillator strip polished. A picture of a finished scintillator strip, can be seen in figure 8.

Figure 7: Sketch of the cross-section of a scintillator strip. All seen dimensions in mm.

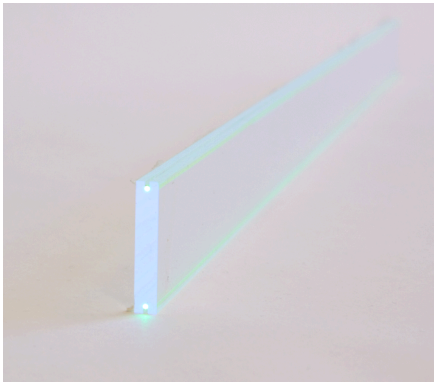

(a) One of the finished scintillator stripes with glued in fibres.

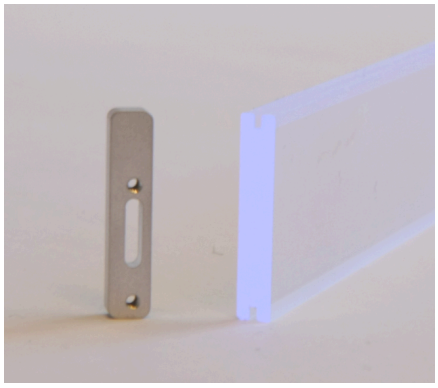

(b) A scintillator blank next to an "island" module. Information on the module can be found in section 4.2

Figure 8: Photos of scintillator strips.

4.2 Casing design

The goal for the design of the casing was to make it possibly portable. In order to connect the light guiding fibres to the readout electronics, it is common to let the fibres extend further out of the scintillator and collect them at a central point [9, 5]. By doing this, the readout electronics are simplified, because not so many daughter boards are needed. Also, the mechanical design is made more simple, since only single fibres need to exit the separate channels. A downside of this setup is its size. Light guiding fibres only allow for fairly large bending radii, of around 10 cm, before they are getting damaged or start losing their light guiding ability [26]. This results in large portions of the casing being used for fibre routing. Since the detector is not meant for mass production and because the portability was desired, the more complicated but more compact setup, with the light detection right at the scintillator, was chosen.

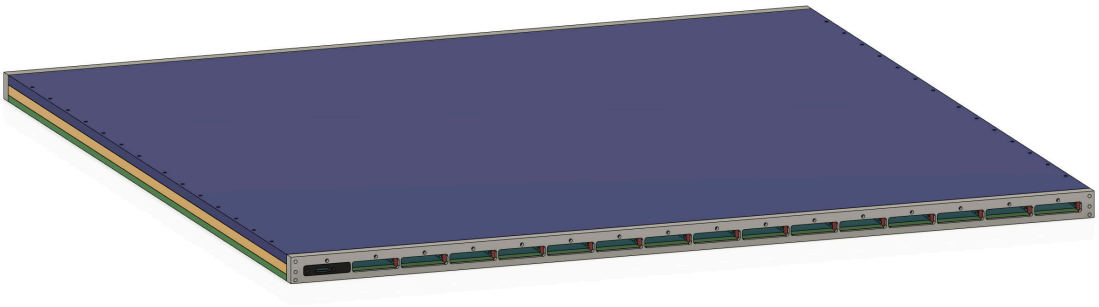

Figure 9: Overview of the whole casing. Detailed renderings of individual parts are shown in figure 10 and 11. The rendering is an isometric projection.

Renderings of the casing's 3D model are shown in figures 9, 10, and 11, respectively. In figure 10 the casing without its faceplate can be seen. The main body consists of two main parts, the lid which is designed to be removable and the bottom which is made of the glued together dividers, exterior walls and the bottom plate.

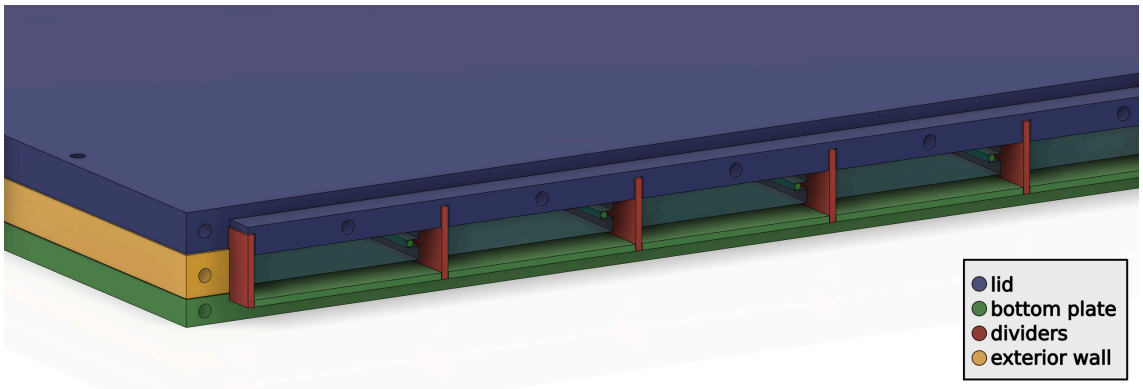

Figure 10: Rendering of the casing without the faceplate. Shown in blue is the lid, in red the dividers, in yellow an exterior wall, and in green the bottom plate, respectively. Inside each channel, a scintillator along with its fibres can be seen.

In figure 10 it can also be seen that the dividers extend into slots in the lid. This design decision, and the protruding of the main body into the faceplate, was made to act as a light trap. These light traps hinder exterior light from getting into the detector. Also, light is blocked from getting from one channel to another. With 55

parts comprising the design, the resulting case got modular and compact.

In figure 11 it is shown how the front end electronics will be integrated into the case. The printed circuit board (PCB) of the front end gets screwed into the faceplate. The SiPM is positioned directly in front of the fibre and the parts of its area that are not covered by the fibre can "see into" the scintillator. The SiPM is coupled to the scintillator by a transparent silicon pad. The design of the PCB is described in section 5.1.

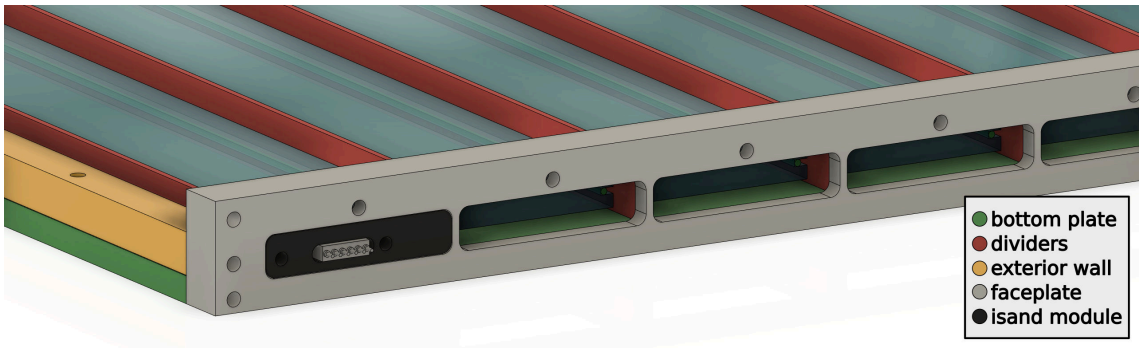

(a) Front view.

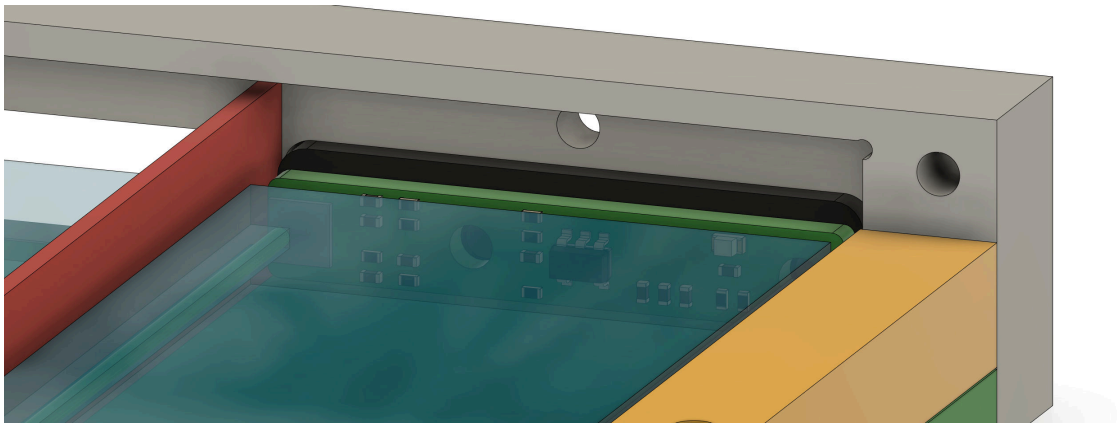

(b) Rear view.

Figure 11: Renderings of the casing without the lid. Shown is in grey the faceplate and in black a island module.

The faceplate is the most intricate part of the casing . This is the reason why, after consultation with the mechanics workshop, it was decided to manufacture the island-like elevations separately. The elevations were implemented as separate

modules which are later glued into place.

In figure 12 and 13 the manufactured aluminium parts can bee seen.

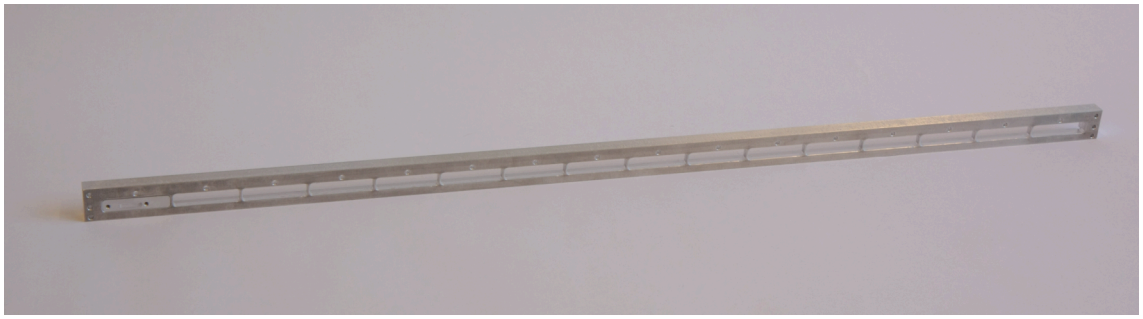

(a) One of the faceplates.

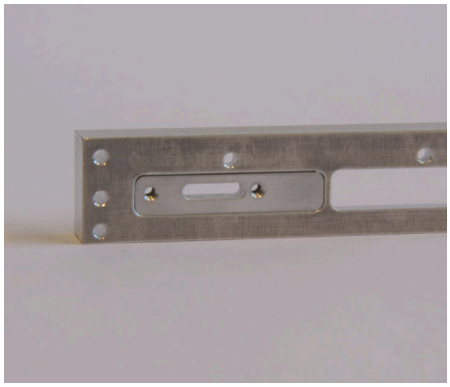

(b) An island module slotted into the faceplate

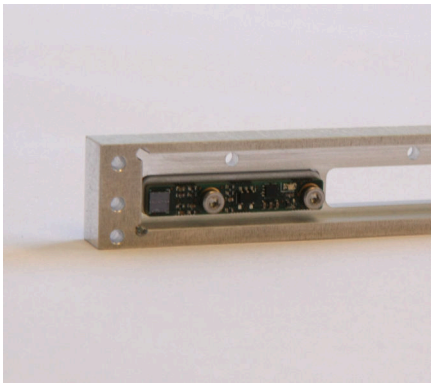

(c) Island module with screwed in PCB. For more information on the PCB see section 5

Figure 12: Photos of manufactured face plate parts.

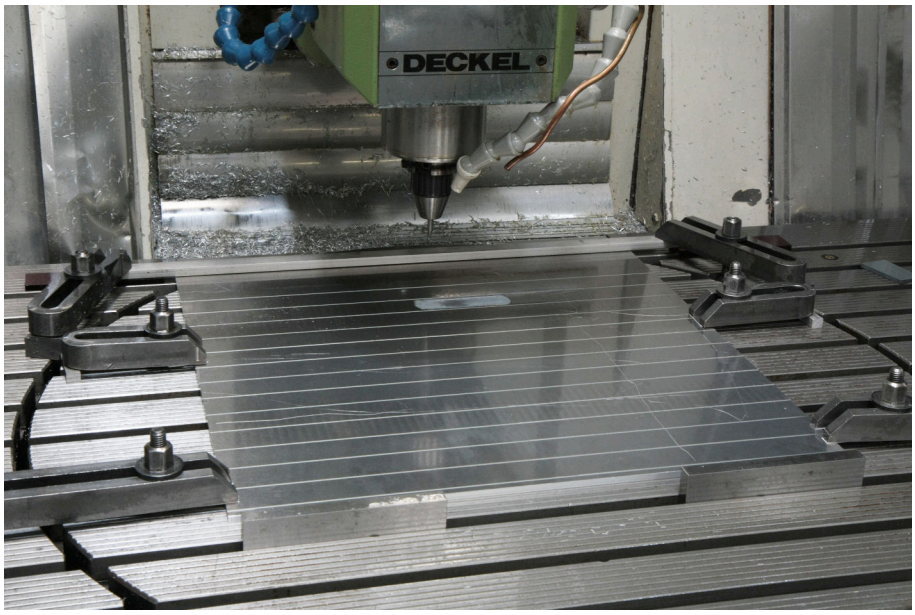

Figure 13: The bottom plate in production.

5 Read-out electronics

This section deals with the design of the front-end electronics and addresses the further processing of the measured signals.

To get an overview of the structure of the data processing, a diagram is shown in figure 14. The front-end board is the first part. It houses the SiPM and its amplifier circuit. Furthermore, it features an UV LED, to be able to generate test light pulses. These light pulses can be used to test and calibrate the SiPMs. The front-end PCB will be integrated into the faceplate of the casing and connected to the carrier board.

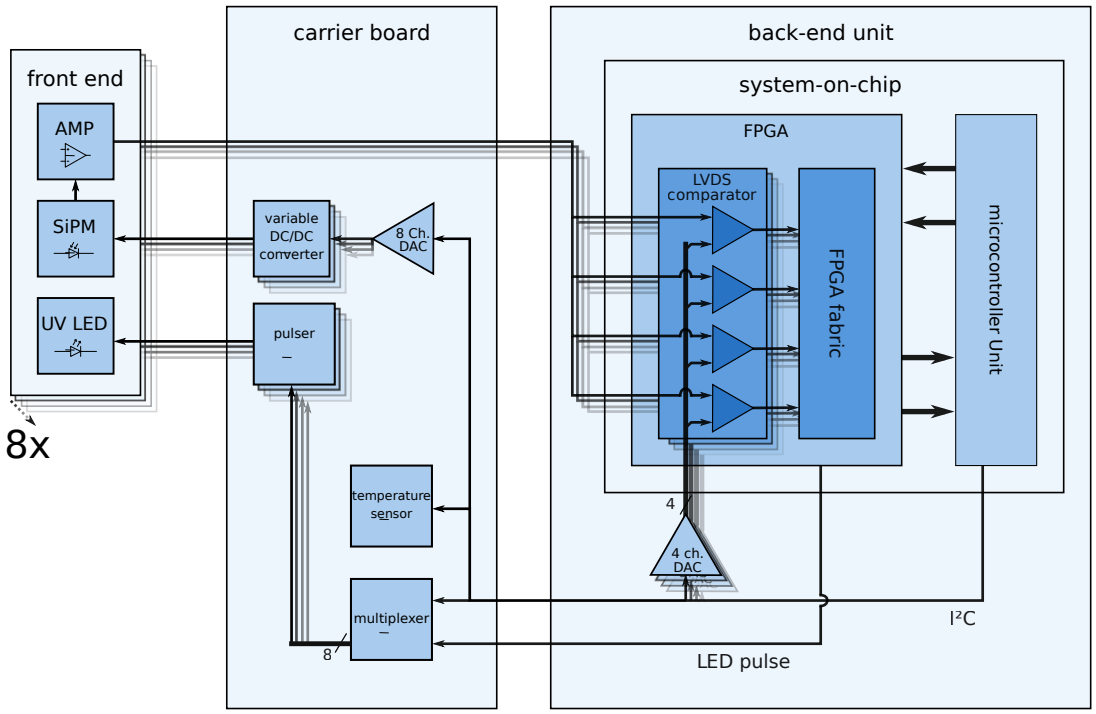

Figure 14: Structure of an eight channel readout module. Each module can control eight SiPMs. For the whole detector, eight of these modules are needed.

One carrier board is connected to eight front-end boards. It supplies the front end with the supply voltage for the amplifier and also hosts a variable DC/DC

converter for every SiPM. Therefore, each SiPM can be supplied with its individual bias voltage. In order to keep track of possible temperature drifts, the carrier board also houses a temperature sensor. Since the LED pulser requires a very short trigger signal, this signal is supplied by the field programmable gate array (FPGA) and directed by a multiplexer. The pulser than supplies a driving signal to the LED.

The data collection and part of the processing is done on the evaluation board. This board hosts a system-on-chip (SoC), which in this case is a integration of an FPGA and microcontroller on the same die. To digitise the signals, a solution used in [29] was chosen. Here, the availability to use the differential modules as inputs to the FPGA is utilised. The typical use of the differential modules is Low Voltage Differential Signaling (LVDS), in our case we aim to use the comparator of the differential input pairs. These comparators are supplied with a reference voltage by DACs and by this can be tuned to trigger at different voltage levels. Per SiPM four of those comparators will be used, together they form a crude ADC. The signals from the comparators get further processed by the FPGA, which in turn sends the resulting data to the SoC-internal microcontroller. The microcontroller is also responsible for the data collection and controls the bias voltages of the SiPMs, the reference voltages of the comparators, the multiplexer for the LED pulse and the temperature sensor.

Within the scope of this thesis only the front-end electronics were designed and built. The design for the carrier board will be made by [30] and the back-end unit was designed by [28].

5.1 Development of the front-end circuit

The 1 p.e. peak of the SiPM is about 0.2 mV high, without amplification and at an overvoltage of 3 V. This is too low for an average oscilloscope to resolve it. In order to be able to distinguish between different p.e. levels, the signal produced by the SiPM needs to be amplified. The discriminability of different p.e. peaks is important for the calibration of the SiPM, as done in section 6. For the calibration of SiPMs on the final detector, this is also needed.

Figure 15 shows a simplified schematic of the amplification circuit used in the front end. An operation amplifier (opamp) in an inverting amplifier configuration was used. The SiPM is connected in series to R_1. When a cell is triggered a current flows through the SiPM and R_1, resulting in a voltage drop at the SiPM. The amplification circuit acts as a high-pass filter. The filtering of the DC part of the signal is important, because the applied bias voltage mostly drops of across the SiPM and would otherwise also be amplified. The used capacitor has a capacitance

of 1 nF and for the resistors $R_2 = 50\,\Omega$ and $R_3 = 680\,\Omega$ are used. The cut-off frequency of this circuit is $f_c = \frac{1}{2\pi R_2 C} \approx 3.2\,\text{MHz}$. This cut-off frequency was chosen to filter most of the noise generated by power supplies. With the chosen resistor values an amplification of $A = -\frac{R3}{R2} = -13.6$ is achieved. Since according to how the SiPM is connected in the circuit, the peaks read out at the SiPM are voltage drops, the amplified peaks will have a positive voltage.

The used op amp is an AD8009 from Analog Devices [31]. It features a maximal small signal bandwidth of 1 GHz and a slew rate of $5500\,\text{V}\,\mu\text{s}^{-1}$, which suits to guarantee the amplification for even the fastest possible SiPM pluses.

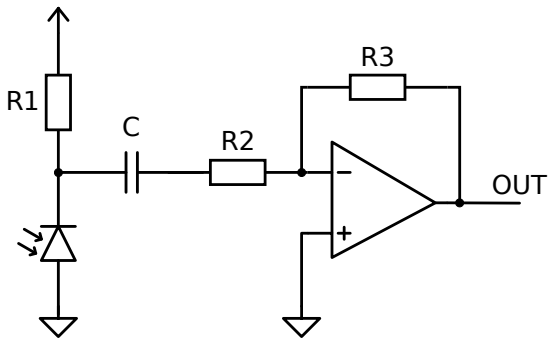

Figure 15: Simplified schematic of the SiPM amplifier. An inverting operation amplifier circuit was used. The complete schematic of the front-end board can be seen in appendix A.

The LVDS comparators of the SoC are designed for signals with a voltage offset [28]. Because of this, the real amplification circuit, shown in appendix A, features a voltage reference. This reference is used to generate a constant offset for the SiPM signal.

In figure 16 a Bode magnitude plot is shown. Here the amplification of the circuit, in dB, can be seen for different frequencies. The plot shows the result of a LTspice [32] simulation in comparison to a measurement taken with a vector network analyser. For the simulation it can be seen that the function has an expected form. Lower frequencies get suppressed with a cut-off frequency of about 3.2 MHz. A maximum amplification of about 22.5 dB gets reached for frequencies between

10 MHz to 100 MHz and for higher frequencies the amplification drops due to the bandwidth of the opamp. The amplification of the real PCB already drops off at a lower frequency, which is expected. Against expectations is the frequency offset of a factor of a about two for the noise filter. At first it was considered a wrong capacitor was used, but this was not the case. At the time of writing this inconsistency is not completely resolved. The impact of this on the operation of the amplifier circuit is negligible, since the exact shape of the SiPM peaks is not of interest.

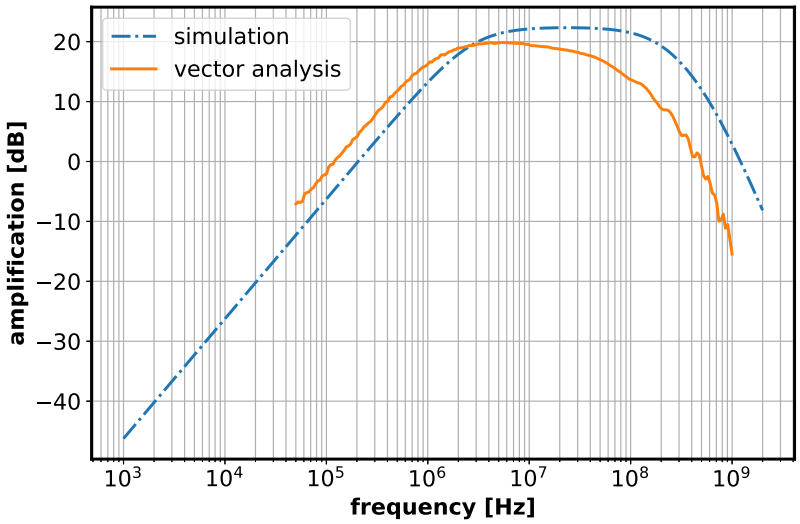

Figure 16: This figure shows a Bode magnitude plot. Shown is a Spice-simulation and the result of a vector analysis of the amplification circuit.

In figure 17 a rendering and a photo of the final PCB can be seen. The PCB of the front end gets integrated into the faceplate of the casing, as discussed in section 4. This imposes the shape and size of the PCB design. The final PCB has a size of 29.5 mm × 5 mm.

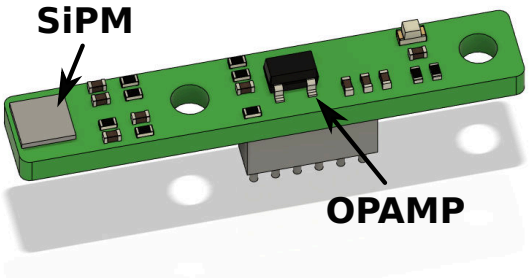

(a) Rendering of the front-end PCB.

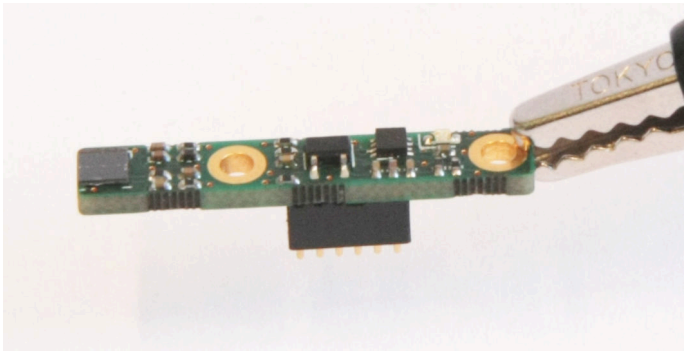

(b) Picture of the finished front-end PCB.

Figure 17: A rendering and photo of the front-end PCB. The SiPM is placed near the left edge of the PCB.

6 SiPM calibration

As discussed in section 2, the breakdown voltage of SiPMs varies between units of the same model and is additionally linearly dependent on the temperature. To be able to achieve the same gain for all 64 SiPMs that will be used in the final detector methods need to be established to calibrate the SiPMs. This section details the process of verifying the slope of the linear function for the breakdown voltage as a function of temperature and development of a method to calibrate the SiPMs during deployment. Furthermore, a suitable voltage and time threshold for coincidence measurements will be calculated.

6.1 Measurement setup

To be able to effectively take measurements with the SiPMs, an automated setup was built. Figure 18 shows a flowchart of this setup. The whole setup is controlled by a Raspberry Pi [33] which controls an oscilloscope, a function generator and a power supply via the virtual instrument software architecture (VISA) API [34, 35]. The power supply, a HMP2030 from Rhode & Schwarz [36], was used to supply a bias voltage to the SiPM and a supply voltage to the amplifier circuit. The amplified signal then got recorded by the oscilloscope, a DSO–X 3034A from Keysight [37]. To trigger the recording of the oscilloscope a signal from the function generator, a AFG3252 from Tektronix [38], was used. By using the signal from the function generator, instead of triggering on the output of the SiPM, unbiased noise could be recorded. The collected waveforms then got transferred from the oscilloscope to the Raspberry Pi. In addition, a temperature sensor, a DS18B20 [39], was connected to the raspberry Pi and placed in the vicinity of the SiPM. The SiPM, its amplification circuit, and the temperature sensor were placed in a dark box, see figure 19.

This measurement setup was used for all calibration measurements. The only encountered downside is the transferring of waveforms from the oscilloscope to the Raspberry Pi. Since the VISA API is not designed for large data transfers, most of the time of a measurement cycle was taken up by the data transfer. The transfer of 1000 waveforms took about five minutes. Since large numbers of waveforms were needed for statistically significant evaluations, measurements took up to three weeks.

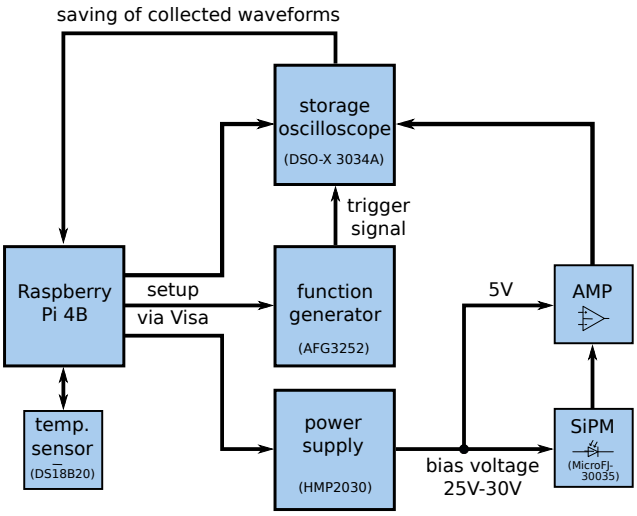

Figure 18: Flowchart of the automated measuring setup.

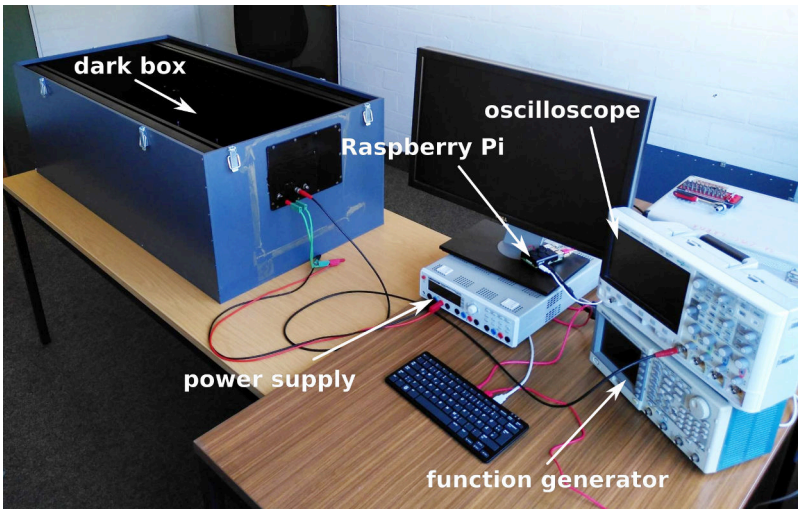

Figure 19: Photo of the automated measuring setup.

6.2 Temperature calibration

In order to measure the temperature dependency of the breakdown voltage, waveforms of noise from the SiPM were recorded at different temperatures. By comparing

the heights of the p.e. peaks, the gain can be determined and compared for different temperatures. Because the setup had no active control of the temperature, different temperatures were archived by normal ventilation from outside. Since the measurements took place over the course of weeks, temperature fluctuation of 8 °C were recorded.

In order to evaluate the collected waveforms, they got transferred to another PC where a python program was used for further data processing. The first step of data processing is a peak finding function [40]. This function identifies peaks in the waveforms and determines their position and height. Figure 20 shows the result of the peak-finding function.

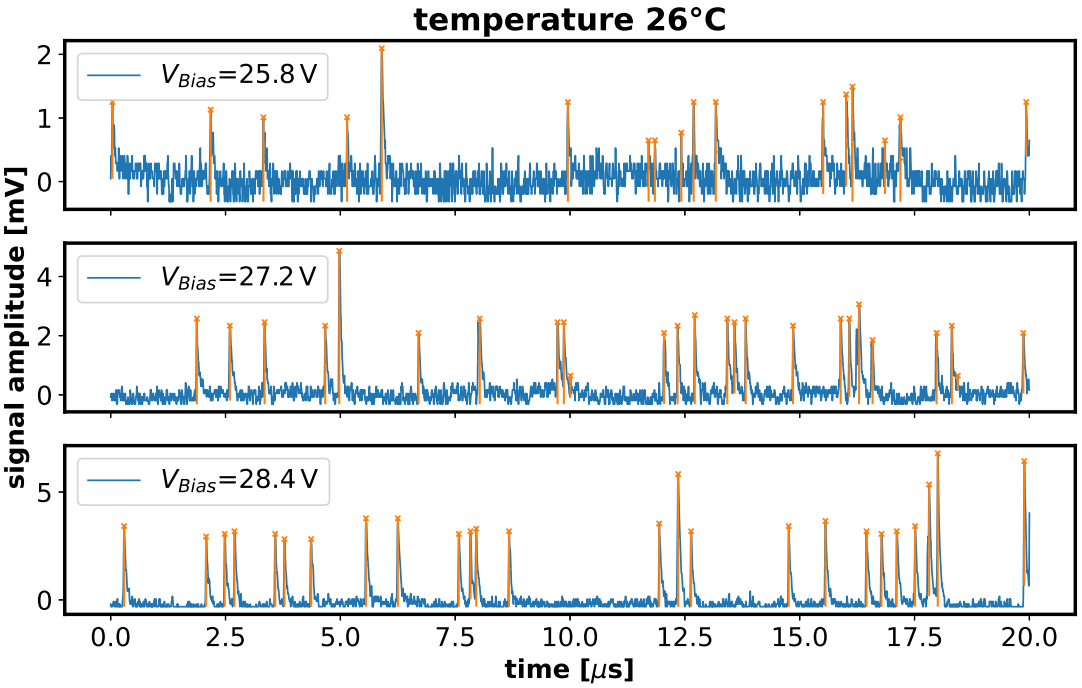

Figure 20: The figure shows waveforms of SiPM noise, which got collected at different bias voltages, at a temperature of 26 °C. Shown in orange are the results of the peak finding.

Waveforms got collected for 16 different bias voltages, starting at 25.8 V up to 28.8 V, in 0.2 V steps. For each bias voltage, 152 000 waveforms got collected which, at a length of 20 µs per waveform, results in a total of 3.04 s of collected noise per

voltage. All waveforms combined had a size of about 200 GB. To be able to analyse this amount of data in a reasonable time span, the evaluation program needed to be reprogrammed to allow for multithreading. The multithreading allowed to reduce the analysis time to a few hours. Histograms, in the form of heat maps, of the peak heights, for different voltages and temperatures, are shown in figure 21.

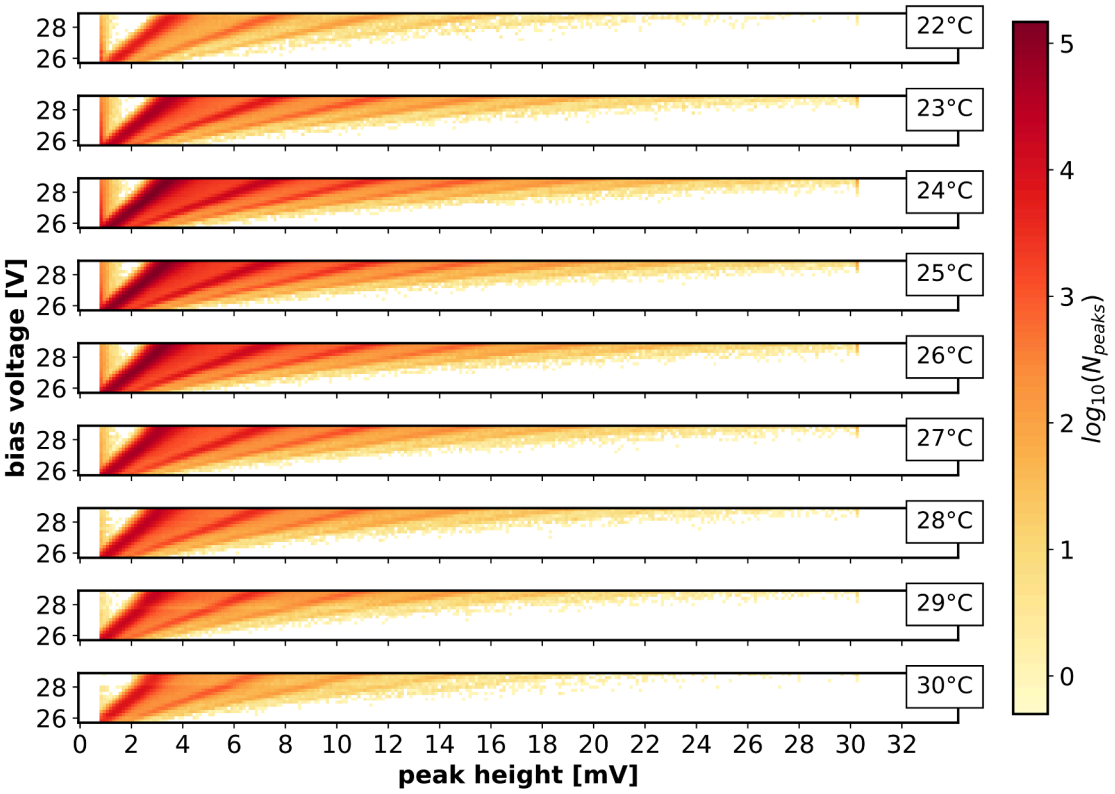

Figure 21: Histograms of the peak heights, from SiPM noise, in the form of heat maps, for different temperatures. On the x–axis the peak height is plotted, on the y–axis the bias voltage. By this, each row of pixels corresponds to one bias voltage. On the right side a colour bar shows the scale of the heat map, which scales logarithmically with the number of peaks.

In figure 21 it can be seen that for the temperatures around 25 °C the highest number of peaks got recorded, this is a consequence of the "weather-controlled" temperature range. Most of the measurements were made during a temperature around 25 °C and only few got recorded at the extremes of 22 °C or 30 °C.

In the plot, the different p.e. peaks can be distinguished as the dark lines. The 1 p.e. being the leftmost. The rise in gain for higher bias voltages can be identified as the drift to higher voltages of the p.e. peaks. The cut-off threshold at 0.8 mV is an artefact of the peak finder, which only counted peaks higher than this voltage, to filter unwanted noise. Some of this noise can still be seen above the threshold. On the right end of the histograms, at 30.2 mV, the end of the voltage range of the oscilloscope is reached, peaks higher than this got cut off resulting in an accumulation of peaks at this height.

The next step of the data processing was to determine the position of the p.e. peaks. This was done by running a peak finder on the histograms shown in figure 21. For higher bias voltages, up to five p.e. peaks can be identified, for the lowest voltages only two could be made out. The results of such a peak find are shown in figure 22.

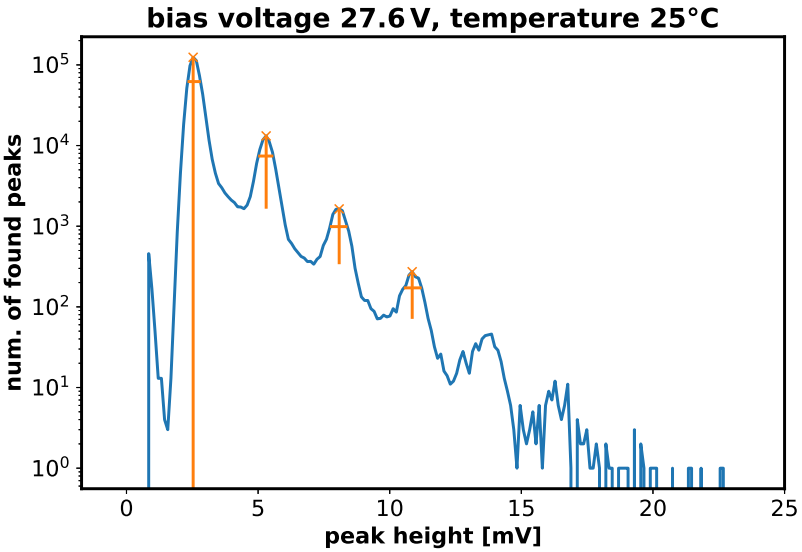

Figure 22: A histogram of the collected peak heights and the results of a peak find on this histogram. This figure shows the same data as the 27.6 V row in the 25 °C plot of figure 21 in the form of a standard histogram instead of a heat map. This peak height histogram of SiPMs is also known as the finger spectrum, due to its characteristic shape.

The uncertainties of the position of the peaks were assessed to be $\sigma_{peak} =$

$0.121\,\mathrm{mV}/\sqrt{12} = 0.035\,\mathrm{mV}$, under the assumption of a uniform distribution over one digitisation step of 0.121 mV. The relative errors of the bias voltage were insignificant in comparison to the one of the peak position and were neglected.

Linear regressions were performed on the data points of peak heights for 1, 2, and 3 p.e. and the bias voltages at which they were measured. One of the linear regressions is shown in figure 23.

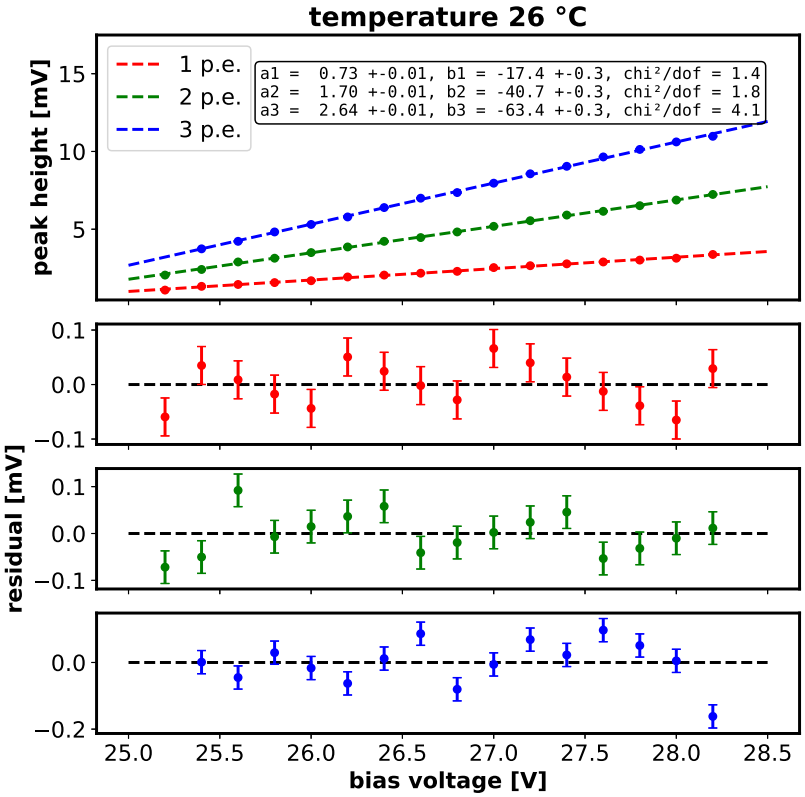

Figure 23: Result of three linear regressions to the peak heights of the 1, 2, and 3 p.e. peaks at different bias voltages can be seen. In the main plot the data points and fit results, for a function of the form $y = a_i x + b_i$, are plotted. The shown values for a have the dimension of 10^{-3} and the values for b are given in mV. At the lower part, the residuals of the fits are plotted.

The the values for the χ^2/dof of the fits indicate that the evaluated errors

represent the observed fluctuation of the values. The well matching fit is also a confirmation that the gain rises linearly with higher overvoltage. Furthermore, for lower temperatures at lower bias voltages only the 1 p.e. and 2 p.e. peaks could be read out from the histograms.

The height of the 1 p.e. or the difference between two neighbouring peaks is proportional to the gain. Because it is possible that the measured voltages feature an offset, the difference between the 1 p.e. and 2 p.e. peak were chosen for further processing. In the following sections this difference is called the $\Delta_{p.e.}$. For each temperature, the difference between the linear function for the two peaks was calculated and is plotted for every other temperature in figure 24. The opaque fringes around the plotted lines represent the uncertainties of the values. Over all temperatures a clear trend is visible that, at the same bias voltage, the gain is lower for higher temperatures.

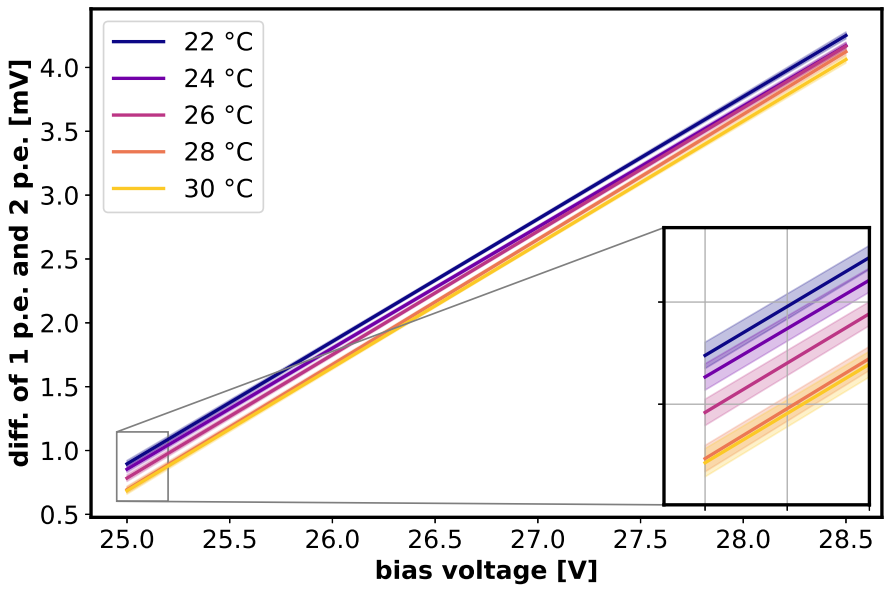

Figure 24: Difference between the 1 p.e. and 2 p.e. peaks as a function of the overvoltage for different temperatures.

Right at the breakdown voltage, the gain of the SiPM is practically zero and from this point on rises with higher overvoltage. The calculated linear functions shown in figure 24 can therefore be extrapolated to the point where they reach zero,

and by this the breakdown voltage at a given temperature can be determined. The extrapolation is shown in figure 25. On the left side, the lines from plot 24 can be seen, extended to the point where they cross zero. The right side of the figure shows data points of the calculated breakdown voltages at the different temperatures and a fit to those points.

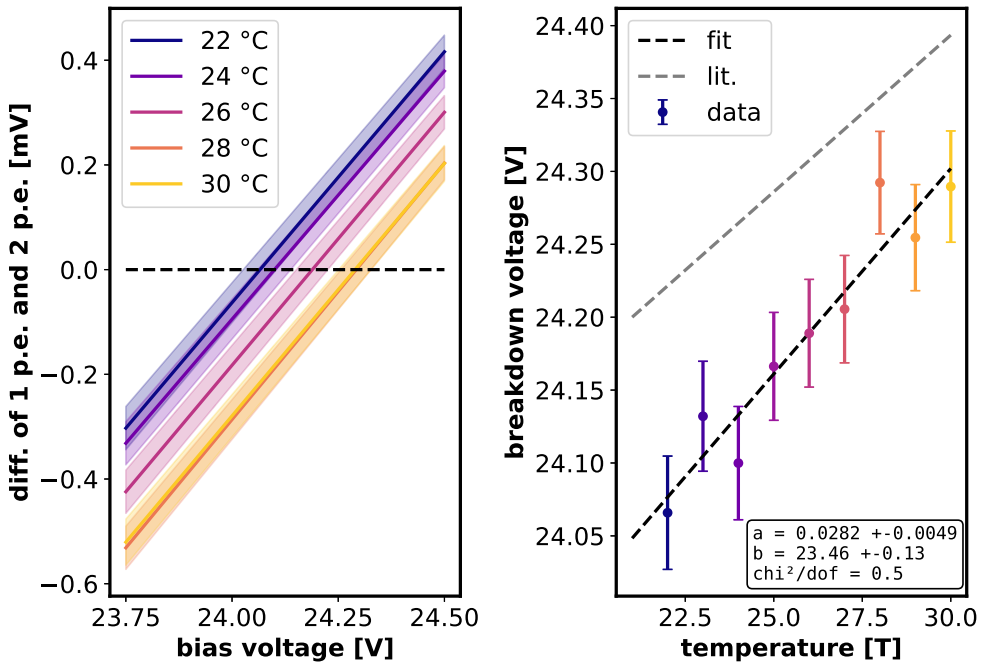

Figure 25: On the left side, the extrapolation of the linear functions from figure 24 can be seen, down to the point where they reach a $\Delta_{p.e.}$ of zero. On the right side, the breakdown voltages are plotted for different temperatures. Thees breakdown voltages were determined by calculating the points where the gain reaches zero, shown in the left plot. Furthermore, the right plot shows a line representing the expected value from the data sheet of the SiPM [19] and the results of a linear regression, of the function $y = ax + b$, on the data ponts. The resulting values are $a = 28.2(49)\,\mathrm{nV\,°C^{-1}}$ and $b = 23.46(13)\,\mathrm{V}$.

Figure 25 shows that the measured data has an offset to the temperature dependence line given by the manufacturer. The reference line has a slope of $21.5\,\mathrm{mV\,°C^{-1}}$. Since the breakdown voltage varies between different units of the same type of SiPM this offset is expected.

For the fit only the uncertainties of the breakdown voltages were utilised and none for the temperature data. The manufacturer of the temperature sensor states the systematic error to be $\pm 0.5\,^{\circ}\mathrm{C}$. For the fit we are only interested in the slope of the linear function, which would be unaffected by this systematic offset. The statistical uncertainty of the temperature measurement had much lower relative uncertainty compared to the one of the breakdown voltage, which made them not of interest.

The fit on the data provides a temperature dependency of the breakdown voltage of $28.2(49)\,\mathrm{mV}\,^{\circ}\mathrm{C}^{-1}$. The whole measurement and analysis were repeated for another SiPM with the result of $33.8(91)\,\mathrm{mV}\,^{\circ}\mathrm{C}^{-1}$. The weighted sum of both calculated values results in $29.5(43)\,\mathrm{mV}\,^{\circ}\mathrm{C}^{-1}$. This result has a high relative uncertainty and the value given by the manufacturer, $21.5\,\mathrm{mV}\,^{\circ}\mathrm{C}^{-1}$ [19], lays within its 2σ interval. With this known temperature dependency, it is now feasible to implement a regulation for keeping a possibly constant gain of the SiPM during a temperature change.

6.3 Calibration method

When all the SiPMs are installed into the detector, another way of determining the breakdown voltage is needed. This calibration is important in order to be able to supply the same overvoltage to all SiPMs.

As discussed in section 5, the read-out electronic does only have four digitisation steps. The generation of a finger spectrum, the way it was done in the previous section, requires a ADC with many digitisation steps. In order to calculate the finger spectrum with the read-out electronics, an alternative procedure was proposed. Instead of measuring the peak height, the trigger rate can be measured as a function of the threshold voltage. By this, obtaining information on the voltage difference between two peaks. A demonstration of this is shown in figure 26. Here, the trigger rate was calculated for different trigger heights. It can be seen, that every time the trigger height surpasses a p.e. peak it drops off and then decreases only slowly, until the next drop-off.

In order to calibrate an SiPM, the position of the trigger rate drop off between the 1 p.e. and 2 p.e. and between the 2 p.e. and the 3 p.e. peaks needs to be measured. The voltage difference between the two drop–offs is proportional to the gain and this in turn is proportional to the overvoltage. The current read out setup ensures the possibility to implement this solution.

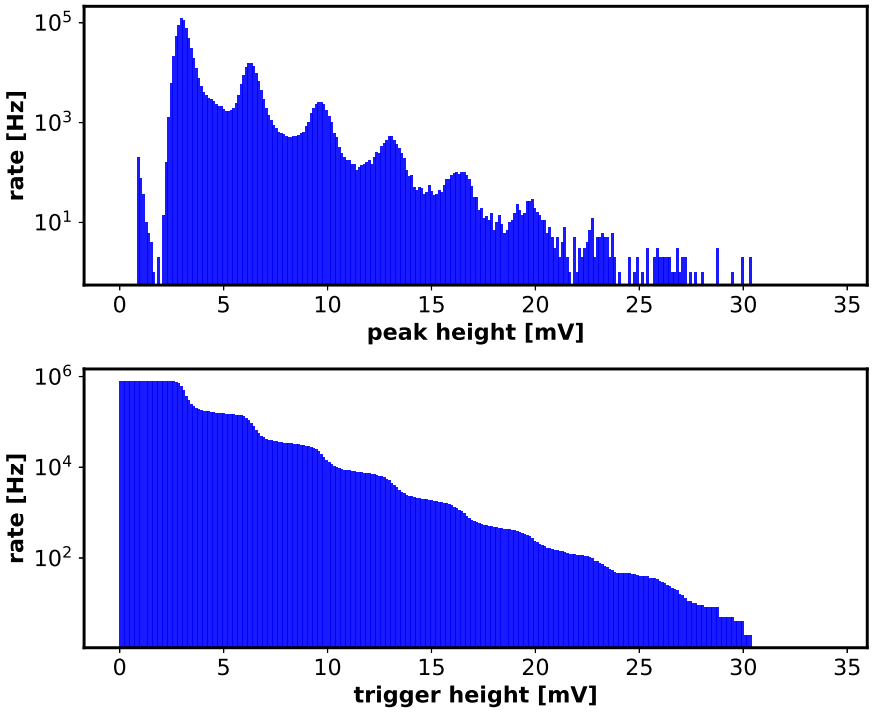

Figure 26: The upper plot shows a histogram of peak heights, for a temperature of 26 °C and a bias voltage of 28.2 V. The lower plot shows the expected trigger rate for a given trigger height, which was calculated from the data of the first plot. This was done by adding up all bins higher than the chosen trigger height.

6.4 Time and Voltage threshold for coincidence measurements

When a particle hits the scintillator and a light pulse is emitted, depending on where the muon hit, the light will not reach the two SiPMs at the ends at the same time. In order to determine if pulses recorded from the SiPM could originate from the same particle, an estimation has to be made what the maximum time difference between two recorded peaks can be.

A scintillator strip is 50 cm long and has a refractive index of 1.58, for the wavelength of the scintillated light [21]. The used fibre has a refractive index of 1.59, for the light that it emits. In the case that a particle hits the scintillator right in front of one of the SiPMs the time it take for the light pulse to get to the other

SiPM is at least 2.63 ns. If we account for the photons that get reflected at the end of a fibre, this time doubles. Depending on the peak height the slope of the rinsing edge of a peak can be different. The total rise time of a peak is, also depending on its height, is about 10 ns to 20 ns long. Accounting for some overhead for the readout electronics, a conservative estimation for the maximum time difference the SiPM signals can have is 20 ns.

In order to decide what the trigger threshold for coincidence measurements should be, it must be determined how high the chance of two noise peaks from two different SiPMs, being close enough together in time to be counted as a coincidence hit, is. In order to calculate this probability, Monte Carlo simulations were performed. In this simulations, the noise of a SiPM at a given noise rate was simulated. Then, single noise events of a second SiPM with the same noise rate got calculated. When two noise peaks had a time difference of 20 ns or less they were counted as a coincidence.

The noise rates which needed to be simulated were derived from the measurements analogous to the trigger rate calculation shown in figure 26. For this simulation measurements at 25 °C were used, because for this temperature the largest amount data was available. Trigger heights slightly above the voltage levels of the 1 - 5 p.e. peaks got simulated. The resulting noise coincidence rates are plotted in figure 27. The data of the noise coincidence rates are only to be taken as first projections and need to be verified once the detector is operational.

At the chosen size of scintillator strips, the expected rate of muons is about 3 Hz [41]. If we demand to have only one noise-induced coincidence in 1000 recorded coincidences, the noise coincidence rate needs to be of the order of 10^{-3} Hz. The data of figure 27 indicates that only trigger heights of 4 or 5 p.e. come into question, and this at a bias voltage below 27.5 V.

In order to get a first estimation at which height the SiPM signals produced by muons are, a measurement was made with a test scintillator coupled to the SiPM. The test scintillator had a dimension of 50 cm × 2.5 cm × 0.5 cm, was wrapped in Tyvek and had only one fibre which was not covered by a reflective material at its open end. The peak height histogram of this measurement can be seen in figure 28. The plot shows the logarithmically decaying SiPM noise and a cluster of peaks slightly higher than the noise, with single peaks reaching higher voltages. As a reference, the 1 - 5 p.e. peak heights are plotted as dashed lines. It can be seen that the 4 and 5 p.e. peaks are right next to the peak cluster and presumably in its tail. In order to be able to measure as many muons as possible, the trigger threshold should be as low as possible. To achieve this, while still retaining a low noise coincidence rate, the bias voltage needs to be lowered. But as discussed in

section 2, the PDE of the SiPM decreases significantly with lower overvoltage.

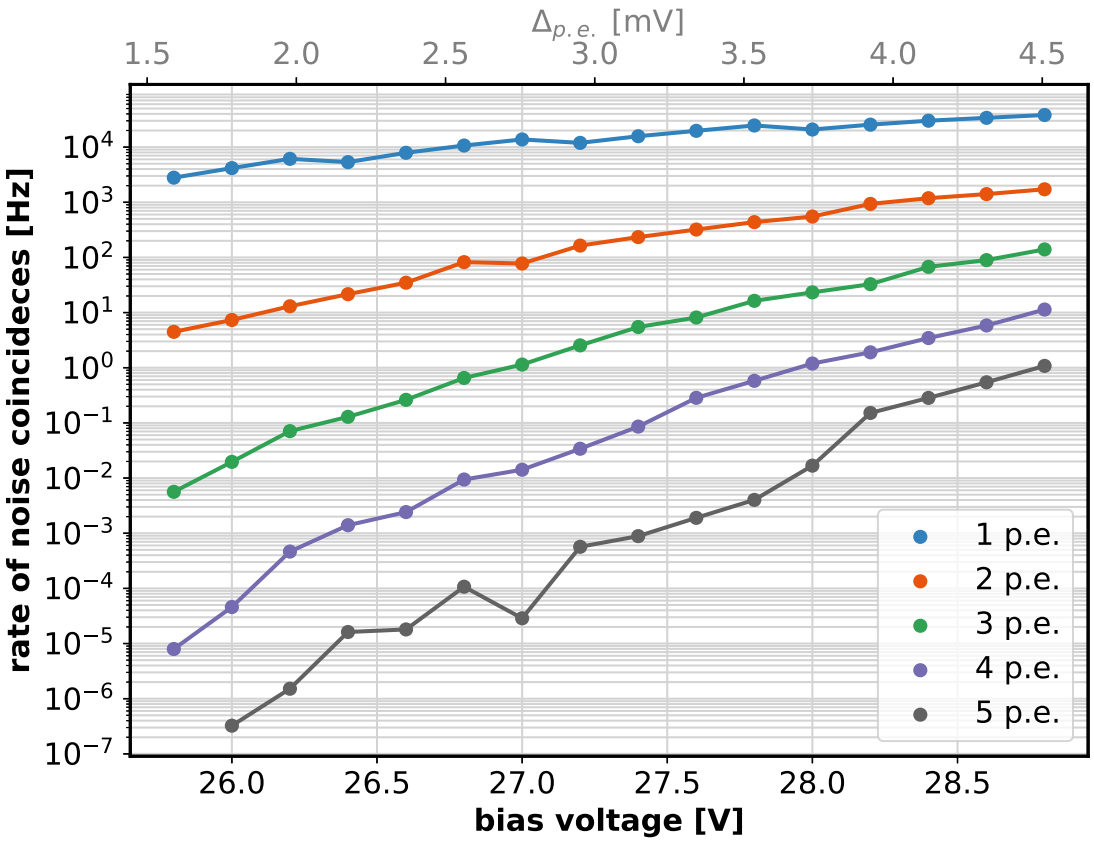

Figure 27: The results of the Monte Carlo simulation for the noise coincidence rates. The rates are plotted for different bias voltages and for different trigger heights. The chosen trigger heights are abased on the positions of the first five p.e. peaks. The x–axis has two scales: one is the applied overvoltage and the other is the $\Delta_{p.e.}$. The $\Delta_{p.e.}$ is proportional to the gain and the overvoltage, and was calculated from the bias voltage with the function shown in figure 24. This could only be done because the function got calculated for the same SiPM from which the noise data for the simulation was taken. This conversion from bias voltage to $\Delta_{p.e.}$ has however a non-negligible uncertainty. Here it was used to demonstrate that it is possible to derive an optimal $\Delta_{p.e.}$ from the shown data, which can be used for the calibration described in section 6.3.

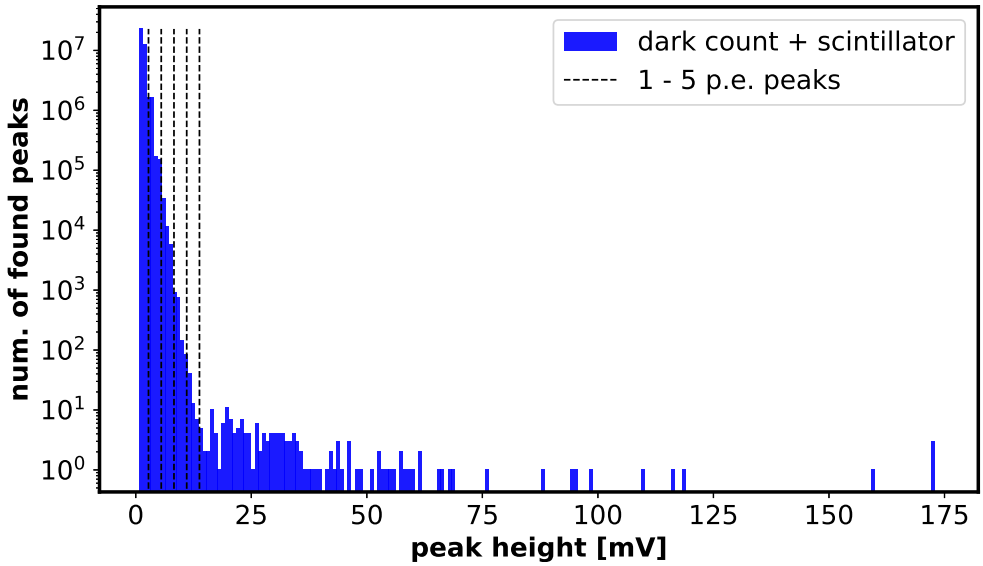

Figure 28: The peak height histogram of a measurement with a scintillator coupled to the SiPM, at a bias voltage of 27 V. To gain more data points, all temperatures were binned together. The shown peaks represent a total measurement time of 81.6 s.

A possible workaround, for the trade-off between overvoltage and trigger height, coincidence matches can not only be made between the two SiPMs of the same channel but also between the different channels of the two layers. This would reduce the noise coincidence rate significantly, and thus allow for a greater overhead for the overvoltage and trigger height combination. The implementation of this method stands to reason because in order to match the channels a muon passed through, to get the x–y resolution, the same matching needs to be made.

The noise coincidence rate for both layers combined was calculated with the same Monte Carlo simulation as the noise coincidence rate of two SiPMs. Here, also 20 ns were chosen as the coincidence window. It is important to note, that a channel can have a coincidence match with all 16 channels of the other layer. The results are plotted in figure 29. In the data, it can be seen that the rates dropped significantly for lower trigger heights. With the same demands, a noise coincidence rate below 10^{-3} Hz and an overvoltage as high as possible, the optimal operating point would be at a trigger threshold at the 3 p.e. peak and an overvoltage with a $\Delta_{p.e.}$ of 3.4 mV. This corresponds to an overvoltage of around 3.45 V.

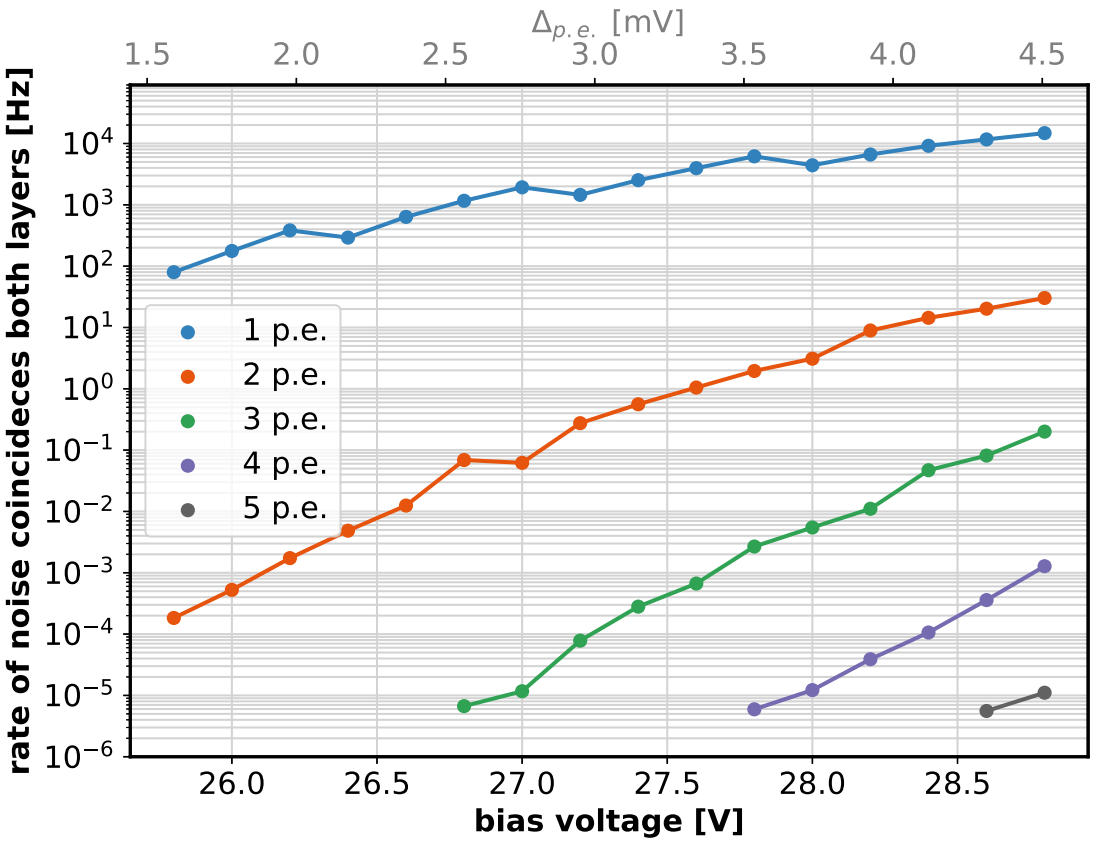

Figure 29: Expected noise coincidence rate if coincidences are matched between both layers of the detector. The rates are plotted for different bias voltages and for different trigger heights. The chosen trigger heights, are the position of the first five p.e. peaks. For the lower voltages and trigger heights no points are plotted, because the rates were so low that no coincidences were found in the simulation. The same notice, made for the second x-axis scale, from figure 27 applies.

7 Summary and Outlook

This thesis presents the development process of a SiPM-based scintillator detector for cosmic muons. The detector is designed to act as a spacial reference detector for calibration of larger scintillator tiles. In order to achieve this spacial resolution a two layer design made out of plastic scintillator stripes was proposed. The base design of the detector's constituents was established.

The detector consists of three main parts, the scintillators, the SiPMs with their read-out electronics, and the casing. During the course of this thesis, a practical way of coupling the SiPM to the scintillators, while integrating them in the casing, was developed. Attention was paid to the maximisation of the photon detection efficiency and possibility to implement coincidence measurements. Contributions were made to the establishment of the detailed read-out chain. The front end for the SiPM was planned and first prototypes of it were tested. First measurements using the front-end electronics were carried out. These measurements verified the information on the temperature dependency of the SiPM, given by the manufacturer. Furthermore, optimal operation parameters for the SiPM were calculated, based on an evaluation of bias voltage and rate of noise-induced coincidences. These calculations are based on noise measurements which were also carried out with the front-end prototypes. In order to calibrate the SiPM in the final deployment, a calibration method is proposed.

Currently, the production of the casing, including the scintillators, is in the final phase. First units of the front end were manufactured. The prototype of the back-end electronics for the reference detector, designed by other colleagues, is produced and the firmware is being developed.

Next steps for the project are first tests on parts of the assembled detector. Here, the determined operation parameters need to be reviewed. In order for the final detector to function, the software for the back end also needs to be programmed. After a successful integration of the hardware, firmware, and software components, the proposed calibration method can be tested.

Literatur

[1] A.P. Ivashkin et al. "Scintillation ring hodoscope with WLS fiber readout". In: *Nuc. Instr. Meth. A* 394.3 (July 1997), pp. 321–331. DOI: 10.1016/S0168-9002(97)00657-8. (Visited on 07/22/2022).

[2] Gergely Gábor Barnaföldi et al. "Portable cosmic muon telescope for environmental applications". In: *Nuc. Instr. Meth. A* 689 (Oct. 2012), pp. 60–69. DOI: 10.1016/j.nima.2012.06.015. (Visited on 07/25/2022).

[3] Andreas Erhart et al. "Development of an Organic Plastic Scintillator based Muon Veto Operating at Sub-Kelvin Temperatures for the NUCLEUS Experiment". In: (2022). DOI: 10.48550/ARXIV.2205.01718. (Visited on 08/03/2022).

[4] Giancarlo Barbarino et al. "A large surface photomultiplier based on SiPMs". In: *Nuc. Instr. Meth. A* 725 (Oct. 2013), pp. 166–169. DOI: 10.1016/j.nima.2012.12.060. (Visited on 08/03/2022).

[5] Satoru Kobayashi et al. "Scintillator Hodoscope with a Few Millimeter Position Resolution for Cosmic-ray Test Stand". In: *PD18*. Tokyo, Japan: Journal of the Physical Society of Japan, Nov. 2019. DOI: 10.7566/JPSCP.27.012009. (Visited on 07/25/2022).

[6] M. C. Recker et al. "Comparison of SiPM and PMT Performance Using a Cs2LiYCl6:Ce3+ (CLYC) Scintillator With Two Optical Windows". In: *IEEE Trans. Nucl. Sci.* 66.8 (Aug. 2019), pp. 1959–1965. DOI: 10.1109/TNS.2019.2926246. (Visited on 07/26/2022).

[7] Srilalan Krishnamoorthy et al. "Design and Performance of a High Spatial Resolution, Time-of-Flight PET Detector". In: *IEEE Trans. Nucl. Sci.* 61.3 (June 2014), pp. 1092–1098. DOI: 10.1109/TNS.2014.2302580. (Visited on 07/25/2022).

[8] Guen Bae Ko et al. "Development of a front-end analog circuit for multi-channel SiPM readout and performance verification for various PET detector designs". In: *Nuc. Instr. Meth. A* 703 (Mar. 2013), pp. 38–44. DOI: 10.1016/j.nima.2012.11.087. (Visited on 07/26/2022).

[9] Igor Yashin et al. "Scintillation hodoscope for muon diagnostics". In: *31st International Cosmic Ray Conference, ICRC 2009* (2009). URL: https://galprop.stanford.edu/elibrary/icrc/2009/preliminary/pdf/icrc1049.pdf.

[10] Claude Leroy and Pier-Giorgio Rancoita. *Principles of radiation interaction in matter and detection*. New Jersey: World Scientific, 2009. ISBN: 978-981-281-827-0.

[11] Zizhao Zong et al. "Study of light yield for different configurations of plastic scintillators and wavelength shifting fibers". In: *Nuc. Instr. Meth. A* 908 (Nov. 2018), pp. 82–90. DOI: 10.1016/j.nima.2018.08.029. (Visited on 08/02/2022).

[12] William R. Leo. *Techniques for nuclear and particle physics experiments: a how-to approach*. Berlin [etc.]: Springer, 1992. ISBN: 978-3-540-17386-1.

[13] Gerhard Lutz. *Semiconductor radiation detectors: device physics*. Berlin: Springer, 2007. ISBN: 978-3-540-71678-5.

[14] S. M. Sze and Kwok Kwok Ng. *Physics of semiconductor devices*. 3rd ed. Hoboken, N.J: Wiley-Interscience, 2007. ISBN: 978-0-471-14323-9.

[15] Stefan Gundacker and Arjan Heering. “The silicon photomultiplier: fundamentals and applications of a modern solid-state photon detector”. In: *Phys. Med. Biol.* 65.17 (Sept. 2020), 17TR01. DOI: 10.1088/1361-6560/ab7b2d. (Visited on 08/04/2022).

[16] D Renker and E Lorenz. “Advances in solid state photon detectors”. In: *J. Inst.* 4.04 (Apr. 2009), P04004–P04004. DOI: 10.1088/1748-0221/4/04/P04004. (Visited on 08/04/2022).

[17] Carsten Andreas Heidemann. “Optical Set-Up for Automatised SiPM Characterisation”. Dissertation. RWTH, 2016. URL: https://publications.rwth-aachen.de/record/660031.

[18] A. Duara et al. “Experimental and extraction procedure for the electrical characterisation of silicon photomultiplier detectors”. en. In: *Nuc. Instr. Meth. A* 979 (Nov. 2020), p. 164483. DOI: 10.1016/j.nima.2020.164483. (Visited on 08/04/2022).

[19] onsemi. *Silicon Photomultipliers (SiPM), High PDE and Timing Resolution Sensors in a TSV package*. 2021. URL: https://www.onsemi.com/pdf/datasheet/microj-series-d.pdf.

[20] W.J. Kindt and H.W. Van Zeijl. “Modelling and fabrication of Geiger mode avalanche photodiodes”. In: *IEEE Trans. Nucl. Sci.* 45.3 (June 1998), pp. 715–719. DOI: 10.1109/23.682621. (Visited on 07/30/2022).

[21] Saint Gobain. *BC-400,BC-404,BC-408,BC-412,BC-416 Premium Plastic Scintillators*. 2021. URL: https://www.crystals.saint-gobain.com/files/1691/download.

[22] DuPont. *DuPontTM Tyvek® 1443R - Product Properties*. 2019. URL: https://www.dupont.com/content/dam/dupont/amer/us/en/microsites/tyvek-design/images/documents/2019-C&I_Tyvek_1443R_Datasheet.pdf.

[23] Simon Nieswand. “Measurement of the exit characteristics of light from optical multimode plastic fibres”. MA thesis. RWTH, 2014. URL: https://web.physik.rwth-aachen.de/~hebbeker/theses/nieswand_master.pdf.

[24] R. Wojcik et al. “Embedded waveshifting fiber readout of long scintillators”. In: *Nuc. Instr. Meth. A* 342.2-3 (Mar. 1994), pp. 416–435. DOI: 10.1016/0168-9002(94)90269-0. (Visited on 07/22/2022).

[25] Daniel Keßler. “Coupling of optical fibers for the Aachen Muon Detector”. Bachelor thesis. RWTH, 2016. URL: https://web.physik.rwth-aachen.de/~hebbeker/theses/kessler_bachelor.pdf.

[26] kuraray. *Plastic Scintillating Fibers Scintillating Fibers Wavelength Shifting Fibers Clear Fibers*. 2014. URL: https://www.kuraray.com/products/psf.

[27] Markus Merschmeyer. *Private communication*. RWTH Aachen University, 2022.

[28] Dmitry Eliseev. *Private communication*. RWTH Aachen University, 2022.

[29] Daoming Xi et al. “FPGA-Only MVT Digitizer for TOF PET”. In: *IEEE Trans. Nucl. Sci.* 60.5 (Oct. 2013), pp. 3253–3261. DOI: 10.1109/TNS.2013.2277855. (Visited on 08/15/2022).

[30] Carsten Presser. *Private communication*. RWTH Aachen University, 2022.

[31] Analog Devices. *AD8009 data-sheet*. 2004. URL: https://www.analog.com/media/en/technical-documentation/data-sheets/AD8009.pdf.

[32] Analog Devices. *LTspice*. 2022. URL: https://www.analog.com/en/design-center/design-tools-and-calculators/ltspice-simulator.html.

[33] Raspberry Pi Ltd. *Raspberry Pi Documentation*. 2022. URL: https://www.raspberrypi.com/documentation/computers/raspberry-pi.html.

[34] PyVISA Authors. *PyVISA*. 2022. URL: https://pyvisa.readthedocs.io/en/latest/.

[35] National Instruments. *NI-VISA*. 2022. URL: https://www.ni.com/de-de/support/documentation/supplemental/06/ni-visa-overview.html.

[36] Rhode & Schwarz. *HMP2030 manual*. 2018. URL: https://scdn.rohde-schwarz.com/ur/pws/dl_downloads/dl_common_library/dl_manuals/gb_1/h/hmp_serie/HMPSeries_UserManual_en_02.pdf.

[37] Keysight. *DSO-X 3034A manual*. 2022. URL: https://www.keysight.com/us/en/assets/7018-02734/data-sheets/5990-6619.pdf.

[38] Tektronix. *AFG3252 manual*. 2015. URL: https://www.manualslib.com/manual/1299496/Tektronix-Afg3000-Series.html#product-AFG3252.

[39] Maxim Integrated. *DS18B20 data sheet*. 2019. URL: https://datasheets.maximintegrated.com/en/ds/DS18B20.pdf.

[40] The SciPy community. *scipy.signal.find_peaks*. 2022. URL: https://docs.scipy.org/doc//scipy/reference/generated/scipy.signal.find_peaks.html.

[41] L. N. Bogdanova et al. "Cosmic muon flux at shallow depths underground". en. In: *Phys. Atom. Nuclei* 69.8 (Aug. 2006), pp. 1293–1298. DOI: 10.1134/S1063778806080047. (Visited on 08/10/2022).

Appendix A Front-end schematic

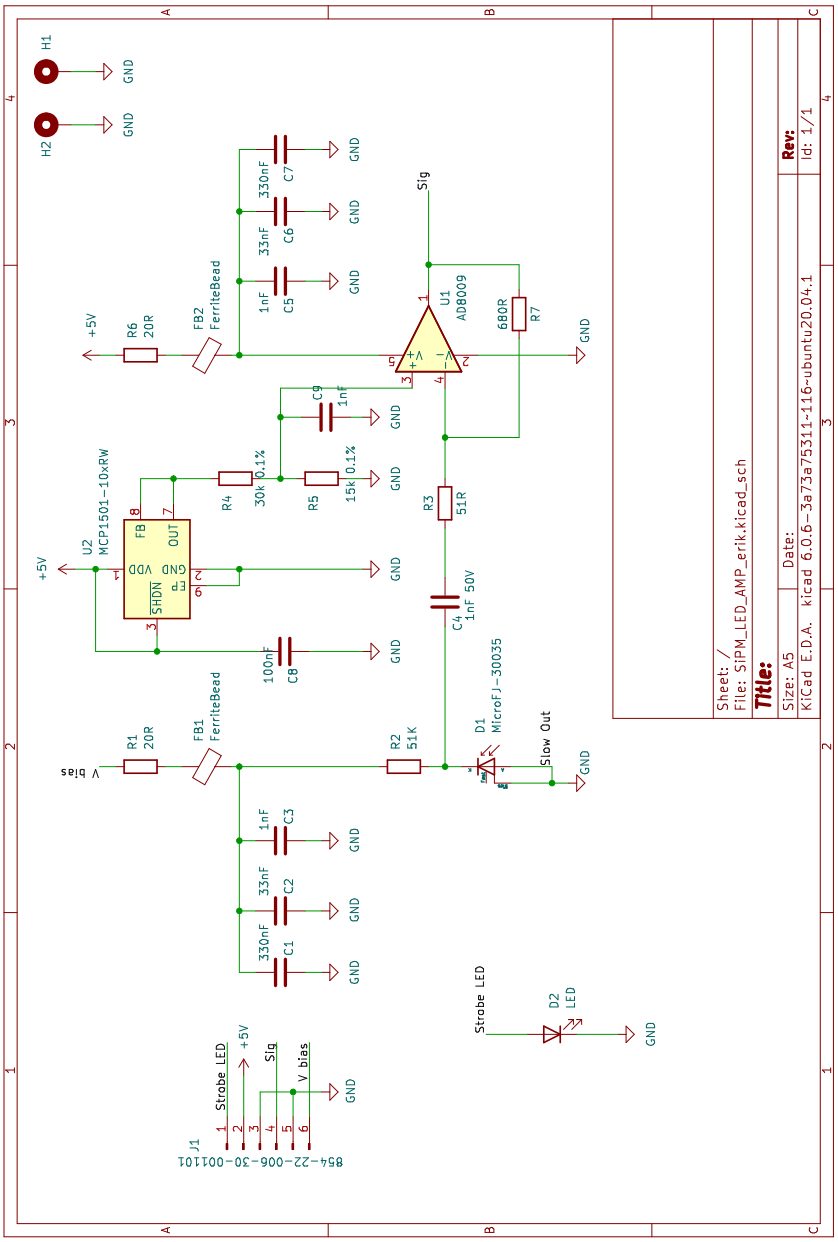

Acknowledgments

I would like to thanks Professor Hebbeker for giving me the opportunity to write my thesis at the Physics Institute III A and likewise Pofessor Pooth for taking the role of the second examiner.
A special thanks goes to Dmitry Eliseev and Markus Merschmayer for supervising and being a constant source of good advice. In addition, i would like to thank them both for proofreading this thesis and offering constructive criticism.
Furthermore does my gratitude go to the electronics workshop and especially to Carsten Persser who helped me in many situation and taught me the basics of KiCad.
Also, I would like to thanks the mechanic workshop, as they assisted the design of the casing and hat a lot of patience with me and my amateurish 3D models.